

# Surface Defect Dynamics in Organic-Inorganic Hybrid Perovskites: From Mechanism to Interfacial Properties

Collin Stecker<sup>†,§</sup>, Kexi Liu<sup>‡,§</sup>, Jeremy Hieulle<sup>†</sup>, Robin Ohmann<sup>†,#</sup>, Zhenyu Liu<sup>‡</sup>, Luis K. Ono<sup>†</sup>, Guofeng Wang<sup>‡,\*</sup>, and Yabing Qi<sup>†,\*</sup>

<sup>†</sup>Energy Materials and Surface Sciences Unit (EMSSU), Okinawa Institute of Science and Technology Graduate University (OIST), 1919-1 Tancha, Onna-son, Okinawa 904-0495, Japan.

<sup>‡</sup>Department of Mechanical Engineering and Materials Science, University of Pittsburgh, Pittsburgh, Pennsylvania 15261, United States.

\*Corresponding authors: Yabing Qi: Yabing.Qi@OIST.jp; Guofeng Wang: guw8@pitt.edu

---

**ABSTRACT:** Organic-inorganic hybrid perovskites (OHPs) have garnered much attention among the photovoltaic and light emitting diode research community due to their excellent optoelectronic properties and low-cost fabrication. Defects in perovskites have been proposed to affect device efficiency and stability, and to have a potential role in enabling ion migration. In this study, the dynamic behavior and electronic properties of intrinsic defects in  $\text{CH}_3\text{NH}_3\text{PbBr}_3$  ( $\text{MAPbBr}_3$ ) were explored at the atomic scale. We use scanning tunneling microscopy (STM) to show unambiguously the occurrence of vacancy-assisted transport of individual ions, as well as the existence of vacancy defect clusters at the OHP surface. We combine these observations with density functional theory (DFT) calculations to identify the mechanisms for this ion motion and show that ion transport energy barriers, as well as transport mechanisms, at the surface depend on crystal direction. DFT calculations also reveal that vacancy defect clusters can significantly modify the local work function of the perovskite surface, which is then expected to alter interfacial charge transport in a device. Our work provides a microscopic insight into the mechanism of ion migration in OHPs, and also delivers the useful information for device improvement from the perspective of interface engineering.

---

**KEYWORDS:** *organic-inorganic hybrid perovskite, scanning tunneling microscopy, density functional theory, ion migration, defects, interface properties*

Organic-inorganic hybrid perovskites (OHPs) have become a main focus for the thin-film solar cell research community due to their advantageous optoelectronic properties, low material cost, and versatility in processing methods. Certified high power conversion efficiencies up to 25.2%<sup>1</sup> have been achieved. However, a substantial trap density has been observed and suggested to influence device performance<sup>2-4</sup> and stability.<sup>5</sup> Defect passivation engineering has been widely employed to reduce defect densities in OHPs.<sup>6-10</sup> On the basis of strategic coordination chemistry employing Lewis base and Lewis acid molecules, different types of defects were proposed to co-exist in OHPs, such as (i) cation-vacancies (*e.g.*,  $\text{Cs}^+$ ,  $\text{CH}_3\text{NH}_3^+ = \text{MA}^+$ , *etc.*),<sup>9</sup> (ii) halide-vacancies (*e.g.*,  $\text{I}^-$  and  $\text{Br}^-$ ) leading to exposure of under-coordinated  $\text{Pb}^{2+}$  ions,<sup>7-10</sup> (iii) metallic lead ( $\text{Pb}^0$ ),<sup>6</sup> (iv) halide-excess (*e.g.*,  $\text{I}_2$ )<sup>11,12</sup> and (v) anti-site  $\text{PbI}_3^-$  defects.<sup>13</sup> Traps can be caused by defects in the crystal lattice, at the perovskite grain boundaries, and/or at the interface between the perovskite layer and adjacent layers,<sup>14</sup> thus understanding the nature of these defects is of great importance for further device optimization and stability improvement.<sup>5, 15</sup> Additionally, density functional theory (DFT) results have shown that Frenkel defects (*e.g.*,  $\text{Pb}^{2+}$ ,  $\text{I}^-$ ,  $\text{Br}^-$ ,  $\text{MA}^+$ ) lead to both deep and shallow trap states in OHPs,<sup>16-19</sup> while Schottky pair defects (*e.g.*,  $\text{PbI}_2$  and  $\text{PbBr}_2$  vacancies and MAI and MABr vacancies) do not

generate trap states within the band gap.<sup>20</sup> Intrinsic vacancy defects have also been suggested to provide pathways for both cations and anions to move within OHPs.<sup>21-24</sup> This ion migration phenomenon has been implicated as a possible cause for material degradation and current-voltage hysteresis.<sup>25,26</sup> Although evidence supporting ion migration in perovskite films and devices has been reported,<sup>27-30</sup> the exact chemical nature of the defects, the mechanism of ion migration, and how this motion affects the local structure, remain elusive.

Understanding defects at the perovskite surface is of particular interest since those defects will have a direct impact on charge transfer properties at the interface between the perovskite film and adjacent layers, typically a charge selective layer or an electrode, in the final device. Interfaces are thought to be a major site of charge recombination<sup>31</sup> and understanding how their structure affects charge transfer is essential for establishing rational interface engineering strategies. Scanning probe microscopy is widely used for characterization of perovskite materials,<sup>32</sup> and scanning tunneling microscopy (STM) has been demonstrated to be an ideal tool to study the atomic structure and stability of the surface of OHPs.<sup>33-36</sup> STM is also a suitable tool for studying dynamics at the atomic scale.<sup>37</sup> STM studies have resolved defects in the perovskite crystal lattice for both  $\text{MAPbBr}_3$  and  $\text{MAPbI}_3$ ,<sup>33,34</sup> and recently theoretical studies

have been performed to address the origin of the intrinsic defects.<sup>38,39</sup> In particular, a theoretical study showed that for MAPbBr<sub>3</sub> the defects visualized by STM are likely MABr or Br<sup>-</sup> vacancies, and that the electronic states associated with them are highly localized around the defect sites.<sup>39</sup> However, defect dynamics in OHPs has yet to be explored with STM. Experimental support for ion migration has been shown at the device level,

but atomic scale verification of this phenomenon and the mechanism at the origin of it is lacking. Here, the nature and dynamics of surface defects in the perovskite crystal lattice, as well as their impact on local electronic properties, are explored *via* a combined study utilizing STM experiments and DFT calculations. Several defect species at the atomic scale are observed, and an atomic scale investigation of ionic motion in OHPs is presented.

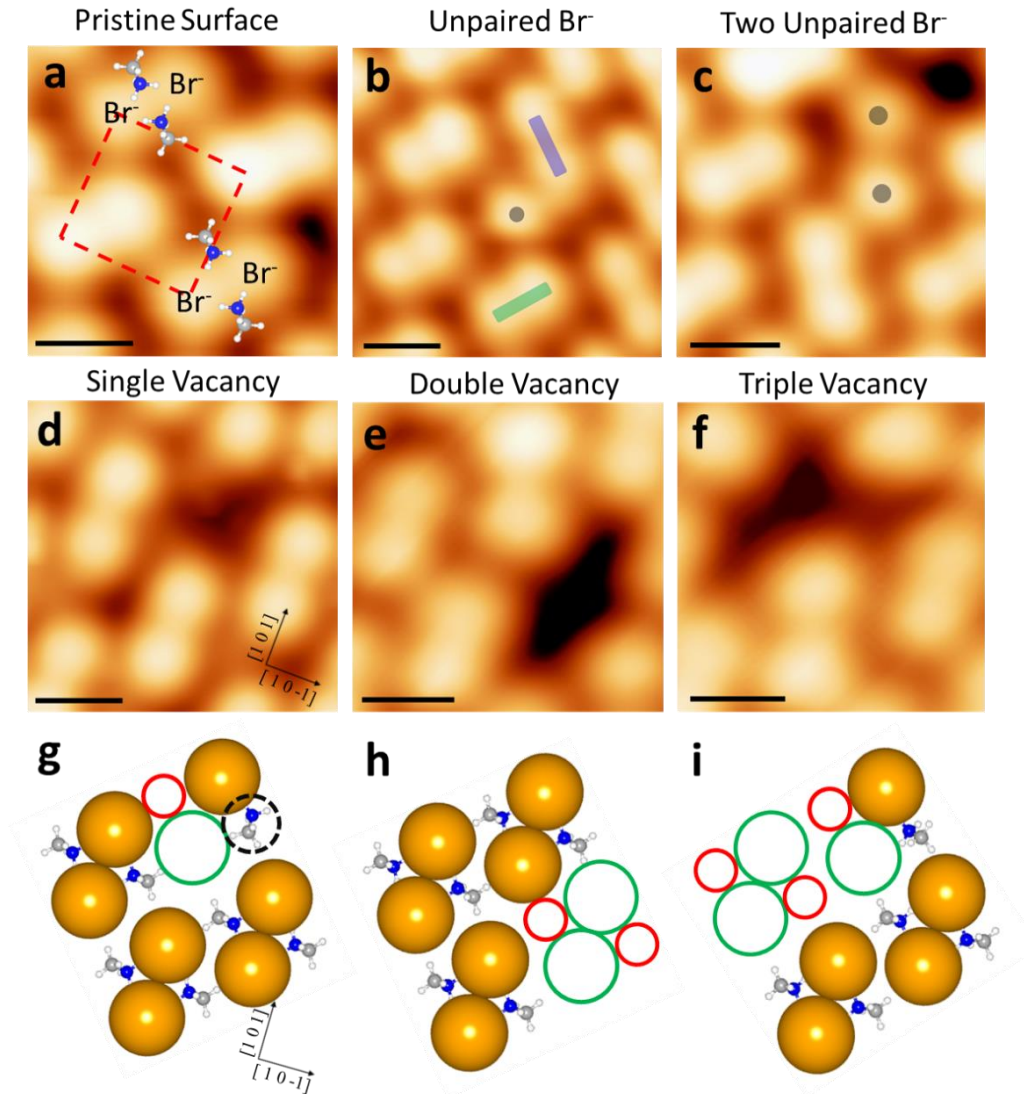


**Figure 1. Intrinsic defects at the atomic scale on the surface of MAPbBr<sub>3</sub>.** (a) STM image of the pristine MAPbBr<sub>3</sub> surface, with MA molecules overlaid to show relative position. The dashed red square denotes the unit cell of the MAPbBr<sub>3</sub> (010) surface. (b) STM image of an unpaired Br<sup>-</sup> (gray dot) at the point where two Br<sup>-</sup> pair orientations (green and blue rectangles) meet. (c) STM image of two adjacent unpaired Br<sup>-</sup> (two gray dots), located near a vacancy. d-f) STM images of single, double and triple vacancy defects, respectively. g-i) Top view of the model slab used for DFT defect formation energy calculations for the single, double, and triple vacancy defect cases, respectively. Solid green and red circles denote Br<sup>-</sup> and MA<sup>+</sup> vacancy locations, respectively. Dashed black circle in (g) highlights a rotated MA<sup>+</sup> molecule. Image sizes: a) 1.6×1.6 nm<sup>2</sup> b) 2.0×2.0 nm<sup>2</sup> c) 1.8×1.8 nm<sup>2</sup> d) 1.8×1.8 nm<sup>2</sup> e) 1.7×1.7 nm<sup>2</sup> f) 1.6×1.6 nm<sup>2</sup>. Imaging parameters: sample bias a-c,e,f) V = -9.0 V d) V = -3.0 V ; tunneling current a-c,e,f) I = 20 pA d) I = 100pA. Sample Type: a-c,e,f) single crystal d) thin film. Color code: N (blue), C (gray), H (white), Br (brown). All scale bars are 5.0Å.

## RESULTS AND DISCUSSION

The work by Ohmann *et al.* showed the surface reconstruction of MAPbBr<sub>3</sub> originating from the relative position and orientations of the dipole of neighboring MA cations.<sup>33</sup> Here, similar STM images of the pristine surface (Fig. 1a) are obtained

on MAPbBr<sub>3</sub> samples prepared by both the single crystal cleavage method and the co-evaporation method (see methods for details). Br<sup>-</sup> ions are seen as bright protrusions in STM images, and the electrostatic interaction of the partially positive nitrogen atoms (blue atoms, Fig. 1a) with two neighboring Br anions

causes “pairing” of the Br<sup>-</sup>. The Br<sup>-</sup> pairs have two possible orientations at the (010) surface, which are orthogonal to each other.

Defects can occur on the paired Br surface, and our STM investigation revealed multiple types of intrinsic defects at the atomic scale. The first defect type is an unpaired Br anion (gray dot in Fig. 1b), which occurs when there is a pair orientation mismatch in the same row (blue and green rectangles in Fig. 1b). The orientation mismatch results in a single Br<sup>-</sup> that has bromide neighbors in each adjacent lattice position, but is paired with none of them. In most cases, the unpaired Br defects are isolated from one another. However, it was also observed that two adjacent unpaired Br defects can occur when there is a vacancy nearby (Fig. 1c). These vacancies constitute the second type of defect observed, and they appear as a dark depression in STM images (Fig. 1d). Here, multiple types of vacancies, including single, double, and triple defects (Fig. 1d-f, respectively) were observed. A recent DFT study provided theoretical evidence showing that these depressions in STM images are likely either a charged Br<sup>-</sup> vacancy or a neutral MABr vacancy.<sup>39</sup>

To further characterize the above observed defects, DFT calculations were performed (see methods for details) considering both MABr and Br<sup>-</sup> vacancies using a 2×2 supercell (Fig. S1).<sup>40</sup> The formation energies for MABr and Br<sup>-</sup> vacancies are calculated by

$$E_{form}(V_{MABr}) = E_{MABr} + E_{V_{MABr}} - E_{MAPbBr_3}$$

and

$$E_{form}(V_{Br}) = E_{Br} + E_{V_{Br}} - E_{MAPbBr_3}$$

respectively, in which  $E_{form}$  is the formation energy;  $E_{MABr}$  and  $E_{Br}$  are the electronic energies of MABr and Br<sup>-</sup> species, respectively;  $E_{V_{MABr}}$  and  $E_{V_{Br}}$  are the electronic energies of the defective MAPbBr<sub>3</sub> surface with MABr and Br<sup>-</sup> vacancies, respectively;  $E_{MAPbBr_3}$  is the electronic energy of the pristine MAPbBr<sub>3</sub> surface. A formation energy of 1.94 eV was obtained for a single MABr vacancy, compared to 2.48 eV for a Br<sup>-</sup> vacancy, suggesting a preference for the formation of MABr vacancies. This trend is consistent with previous calculations in the literature<sup>39</sup>. It is worth noting that these values were obtained without correction for van der Waals forces. To evaluate the influence of van der Waals forces additional calculations were performed and the same trend was found (Table S1). Thus, more complex calculations in this study were performed without van der Waals corrections to save computational time. Additionally, because a neutral MABr vacancy was found to be more energetically favorable (1.94eV), we only consider MABr vacancies in subsequent calculations unless otherwise stated. We do not, however, use this as a basis to rule out the possibility of charged vacancies in perovskite films. Rather, we focus on the neutral defect due to computational concerns related to the influence of image charge in the case of a charged vacancy. For a single MABr vacancy, calculations show that there is a 90° rotation of the MA cation adjacent to the defect (Fig. 1g, dotted black circle), with the positive nitrogen end of the dipole near the unpaired Br<sup>-</sup>. The formation energies for double and triple MABr vacancies were also calculated and found to be 3.49 eV and 5.36 eV, respectively. Having characterized the surface defects observed on the MAPbBr<sub>3</sub> surface, we now focus on the dynamics seen at the surface.

The first manifestation of dynamics at the perovskite surface consists of Br<sup>-</sup> pair reorientation, which was observed in consecutive STM images of the same area. In the (010) surface reconstruction, Br<sup>-</sup> pairs are oriented along either the [101] or [10-1] axes, which are orthogonal to each other (green and blue rectangles in Fig. 2a and b). Strikingly, Br<sup>-</sup> pairs could dissociate and re-associate with neighboring Br<sup>-</sup> ions, thus forming pairs rotated 90° (blue rectangles in Fig. 2b) compared to their original orientation (green rectangles in Fig. 2b). In the case shown in Fig. 2, the reorientation occurs within a single “orientation domain” (*i.e.*, all rows start with the same orientation). Br<sup>-</sup> pair reorientation can also occur at the edge of two orientation domains (Supplemental Movie 1).

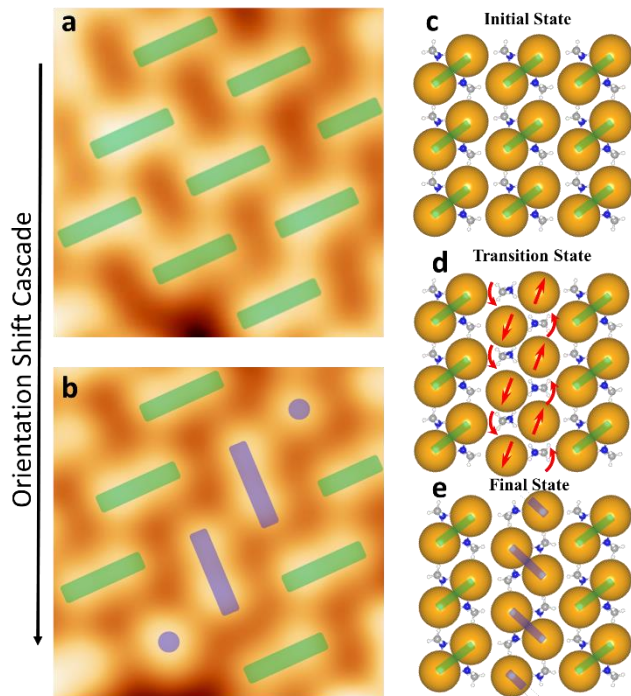


**Figure 2. Br<sup>-</sup> pair orientation shift.** a,b) Consecutive STM images of single crystal MAPbBr<sub>3</sub> showing a Br<sup>-</sup> pair orientation shift. The three rows start in the same orientation (a, green rectangles), but the middle row undergoes an orientation shift to form pairs rotated 90° (b, blue rectangles) from the original orientation. Image size: a-b) 2.3 × 2.3 nm<sup>2</sup>. Imaging parameters: a-b) sample bias voltage = -9.0 V; tunneling current = 20 pA. c-e) DFT simulations of Br<sup>-</sup> dimer reorientation showing the initial (c), transition (d) and final states (e). The transition state energy is 0.31eV higher than the initial and final states, which were found to have the same energy. Color code: N (blue), C (gray), H (white), Br (brown).

A DFT simulation of the Br<sup>-</sup> pair reorientation process was calculated using a 3×1 supercell (Fig. S1) and shows that a rotation of the MA<sup>+</sup> molecules is accompanied by a separation of Br<sup>-</sup> pairs (Fig. 2d). Further rotation in the same direction then results in those separated Br<sup>-</sup> creating a pair with their other neighbor. The initial and final states were found to have the same energy, indicating that there is no preferred orientation for the Br<sup>-</sup> pairs at the perovskite surface. This result is consistent with our experimental observation where the same row may reorient but then later return to its original orientation. In addition to a rotation within an orientation domain as shown in Fig. 2, reorientation events were observed occurring along an orienta-

tion domain boundary (*i.e.*, one of the rows adjacent to the reorienting row is of the opposite orientation). It was found a reorientation event has a lower transition state energy barrier of 0.13 eV when it occurs at an orientation domain boundary, compared to 0.31 eV when it occurs within a single orientation domain (Fig. S2). The lower energy barrier means that reorientation is more likely to occur at the boundary of two orientation domains. Additionally, from experimental observation, reorientation cascades tend to start and terminate more often near defects. DFT calculations comparing separation of a Br<sup>-</sup> pair on a pristine surface *versus* a surface with a vacancy defect suggest that the proximity of a vacancy facilitates the Br<sup>-</sup> unpairing. A lower energy of separation for paired Br<sup>-</sup> was found when the pair is near an MABr vacancy (Fig. S3). This calculation result can explain the two adjacent unpaired Br<sup>-</sup> ions close to an MABr vacancy in Fig. 1c. The calculation shows that the unpairing of the Br<sup>-</sup> ions is also accompanied by a rotation of the MA cation on the defective surface. The MA<sup>+</sup> rotation and Br<sup>-</sup> pair separation are also necessary for allowing the Br<sup>-</sup> pair reorientation event. This suggests that a reorientation event is more energetically favorable when occurring near a vacancy defect. It is worth noting that these reorientations were observed occurring in cascades covering distances on the order of tens of nanometers (Fig S4). Thus, it could be possible that defect movement in one area of the perovskite surface could cause an orientation shift that then affects a remote area of the film.

In addition to Br pair reorientation, MABr vacancy-assisted ion transport along the surface was also imaged. Consecutive STM images (Fig. 3a and b) show mobility of the vacancies along the perovskite surface. Multiple ion transport paths were identified and DFT simulations were performed. Importantly, a substantial difference in energy barrier was found depending on the mechanism. To simulate the ion transport process, a sequential mechanism in which Br<sup>-</sup> moves first, followed later by MA<sup>+</sup>, was envisaged by DFT. In the first step, when Br<sup>-</sup> moves alone, there is a higher transition energy of 0.91 eV and an increase in system energy of 0.14 eV (Fig. 3c-f). This energy increase is likely due to an increase in electrostatic potential energy from the creation of isolated charges. In contrast, when a simultaneous transport mechanism is considered, where MA<sup>+</sup> and Br<sup>-</sup> migrate together, the transition energy barrier is lowered to 0.46 eV and there is no increase in the system energy (Fig. 3g-j). This finding is significant as it suggests that once an MABr vacancy exists at the surface, the MA<sup>+</sup> and Br<sup>-</sup> tend to diffuse together when moving along the (010) surface layer. This result unambiguously shows that defects migrate not just at the grain boundaries, but also along the perovskite interface with other layers in a device. This implies that there is temporal change of local interfaces properties.

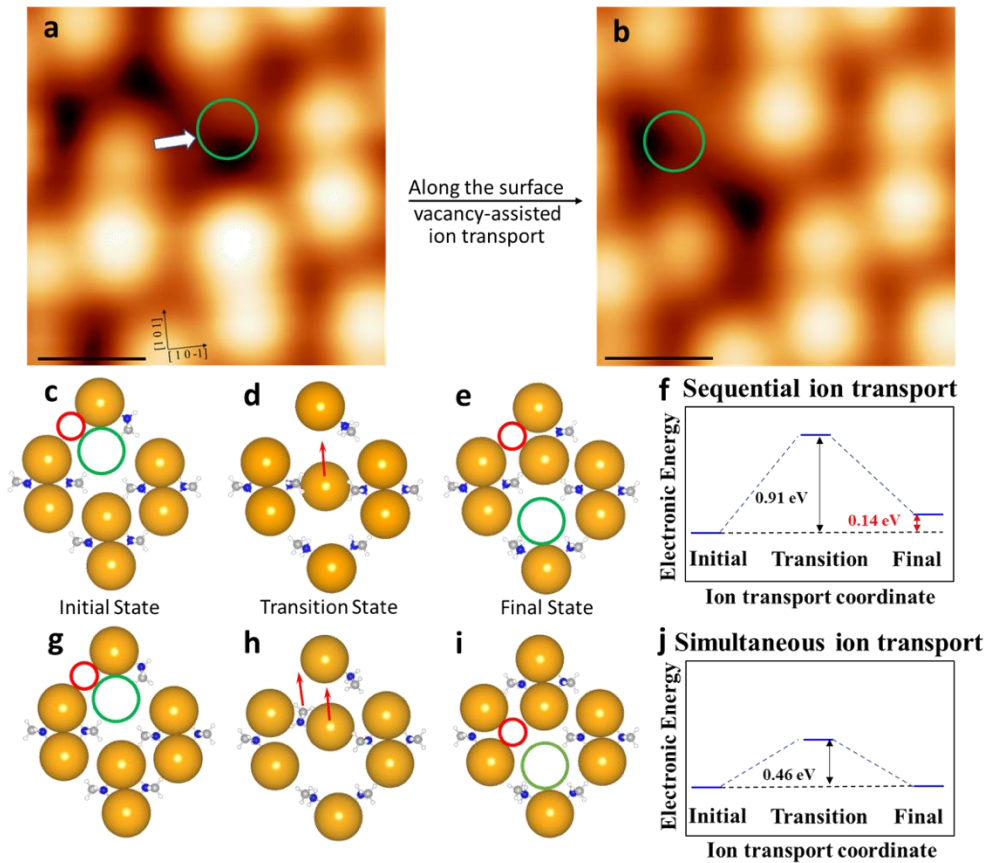


**Figure 3. MABr vacancy-assisted ion transport along the surface of MAPbBr<sub>3</sub>.** a-b) Consecutive STM images showing vacancy defect movement along the surface of an ultra-thin film of MAPbBr<sub>3</sub> at 180 K. Models and energy diagrams calculated *via* DFT of a sequential migration (c-f) and simultaneous migration (g-j) of MABr. The sequential migration is simulated by a Br migration as the first step. Image sizes: a-b) 1.7 × 1.7 nm<sup>2</sup>. Imaging parameters: a-b) sample bias voltage = 1.4 V; tunneling current = 50 pA. Color code: N (blue), C (gray), H (white), Br (brown). Scale bars in a and b are 5.0Å.

Aside from ion transport along the perovskite surface, it was also observed that vacancies and ions can move in the z-direction, through the perovskite film. This is significant since such ion migration has been suggested as a potential cause of hysteresis and material degradation in the device,<sup>25,26</sup> although the mechanism has been unclear. Here, in consecutively recorded STM images (Fig. 4a,b), a single vacancy defect appears at the surface (*i.e.*, the vacancy assists ion transport from the surface to the bulk). This observation strongly supports the hypothesis that these vacancies provide a pathway for ion migration in perovskite materials. The opposite event was observed as well, wherein a single vacancy assists ion transport from the bulk to the surface (Fig. S5), which is consistent with

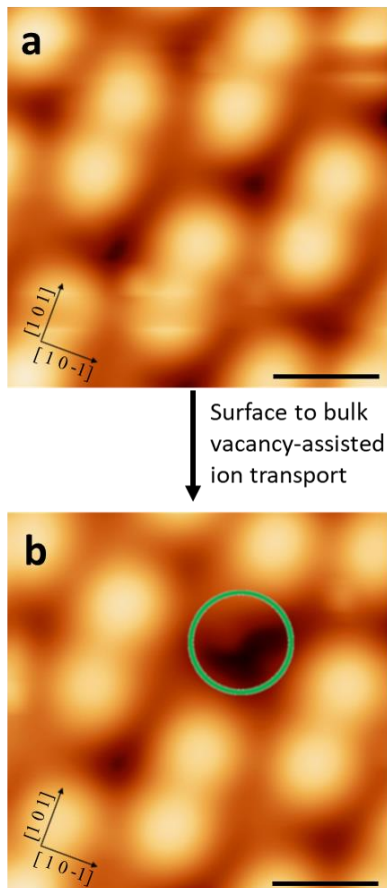


**Figure 4. MABr vacancy-assisted ion transport in Z-direction.** Consecutive STM images acquired at 77K on thin film MAPbBr<sub>3</sub> showing an MABr vacancy-assisted ion transport from the surface layer (a) to the bulk (b). Image sizes: a-b) 1.8 × 1.8 nm<sup>2</sup>. Imaging Parameters: a-b) sample bias voltage = -3.0 V, tunneling current = 100 pA. Color code: N (blue), C (gray), H (white), Br (brown). Scale bars are 5.0Å.

device level measurement indicating ion migration to be reversible.<sup>27,41</sup> Importantly, the fact that the surface layer structure changes means that the interface in a device can change as defects appear and disappear. Although it is challenging to perform a rigorous determination of ion transport event frequency *via* STM, a rough range of one event per 10<sup>1</sup>-10<sup>3</sup> seconds can be estimated based on the STM image acquisition time and line scan speed. More importantly, these events can occur at a much higher frequency at the fabrication and operation temperatures of a device, which are significantly higher than the STM imaging temperatures in this work.

Of the dynamic events observed, the surface to bulk movement is of special interest since it more closely corresponds to the widely studied but not well understood phenomenon of ion migration in perovskite solar cells. One mystery that remains is the mechanism by which ion migration occurs. DFT calculations were performed to identify the possible mechanism of the ion transport observed *via* STM. The calculation considers a cell in which a single MABr vacancy defect exists in the bulk layer. Thereafter, a simulation of the transport of the MABr vacancy was performed. It was found that it is energetically more favorable by 0.75eV for the MABr vacancy to be in the surface layer than in a bulk layer. Simulations of multiple migration mechanisms were tested and it was found that a sequential mechanism is energetically favored (Fig. 5a,b). In this sequential process, a Br<sup>-</sup> ion moves from the sub-surface layer to the bulk layer. This is followed by an MA molecule crossing from the surface layer to the bulk layer *via* the Br<sup>-</sup> vacancy left in the sub-surface layer. Finally, in the last step of the process, a Br<sup>-</sup> ion travels from the surface layer to the sub-surface layer. The energy barrier for a multi-step process is determined by the highest barrier for an individual step. An energy diagram showing the barrier for each step (Fig. 5c) reveals that the highest barrier is 0.55 eV and occurs during the second step, as the MA<sup>+</sup> crosses through the sub-surface layer. Actual computed ion transport energy curves and intermediate crystal structures are shown in Fig. S6 and Fig. S7, respectively. For the reversed sequential mechanism that describes the MABr vacancy migrating from surface to bulk, 1.09 eV is the overall energy barrier. The energetic favorability of the forward sequential mechanism compared to a simultaneous transport mechanism in which MA<sup>+</sup> and Br<sup>-</sup> migrate together (Fig. S8), can be explained by a decrease in steric hindrance. During the first step of the sequential mechanism, the Br<sup>-</sup> vacancy formed in the sub-surface layer provides a larger gap through which the MA<sup>+</sup> can cross the atomic layer. Additionally, this mechanism is sterically favorable because only the MA<sup>+</sup> is crossing the sub-surface layer, rather than the larger MABr passing through the layer as one unit.

It bears mentioning that there was no external stimulus (*e.g.*, external bias, light, temperature, or chemical gradient) considered in our calculations. Many factors are at play contributing to ion transport in an operating device, and multiple pathways for transport have been suggested.<sup>42</sup> The sequential mechanism examined here provides one answer to the question of how ion transport occurs in perovskite films. Ion migration induced by the built-in electric field of devices has been shown to be reversible and the transport seen here can provide clues about how the ions re-establish their original equilibrium distribution after a device is turned off.<sup>24,43</sup> Specifically, we contrast the z-direction ion transport case, where MA<sup>+</sup> and Br<sup>-</sup> move sequentially, with the case of along the surface transport, where the MA<sup>+</sup> and Br<sup>-</sup> ions were found to move simultaneously. Transport along the surface does not require the MA<sup>+</sup> ion to pass through the sterically constrained PbBr<sub>2</sub> sub-surface layer, which allows simultaneous movement of MA<sup>+</sup> and Br<sup>-</sup> to be energetically favorable (Fig. 3c-j). Although our calculation describes cases of ion transport that involve surface layers, some information regarding transport in the bulk can be extracted. The energy profile in Fig. 5c shows that the highest energy transition state occurs when the MA<sup>+</sup> crosses through the sterically hindered PbBr<sub>2</sub> subsurface layer. Such PbBr<sub>2</sub> layers placed deeper into the bulk can also be expected to cause a high transition state barrier for the z-direction, *i.e.*, [010] direction, migration in the

bulk. Although the magnitude of the difference in energy barriers between ion transport along the  $[10\pm 1]$  and  $[010]$  directions may be different for the bulk case, it is reasonable to expect migration along the  $[010]$  direction will have a higher energy barrier, as the hurdle of crossing the  $\text{PbBr}_2$  layer still exists in the

bulk. That energy barrier is expected to increase in the case where an  $\text{MA}^+$  alone is migrating and there is no  $\text{Br}^-$  vacancy nearby to facilitate the crossing of the  $\text{PbBr}_2$  layer, making  $[010]$  migration even less favorable.

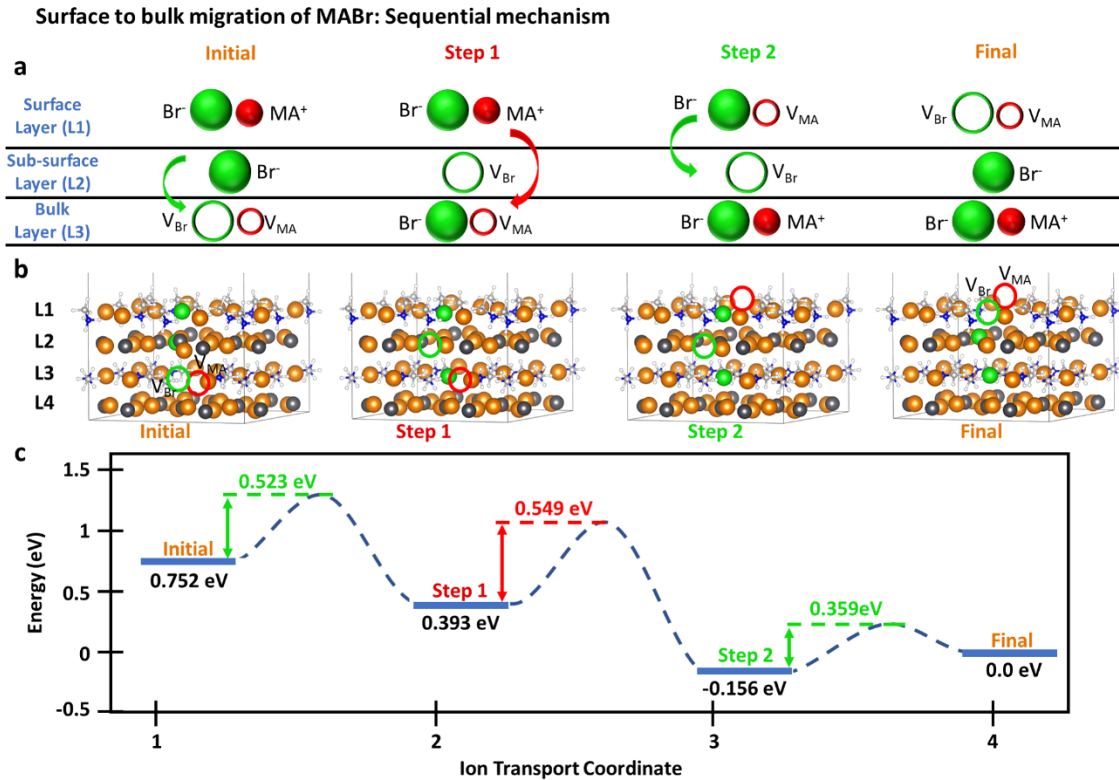
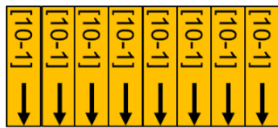


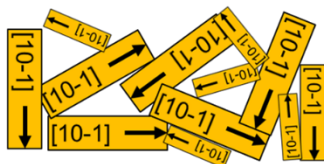
**Figure 5. Sequential migration mechanism.** a) Schematic drawing showing  $\text{MA}^+$  and  $\text{Br}^-$  movement for each step of the mechanism. Empty circles represent vacancies. b) Crystal structures from DFT simulation of the sequential mechanism. Empty circles represent vacancies. c) Illustration of the energy profile for the sequential mechanism showing the energy barrier for each step. The highest energy barrier, and thus the barrier for the entire mechanism, is highlighted in red.

**E-field aligned with preferred direction**



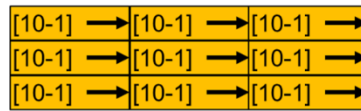
**Quicker stabilization and recovery time**

**Distribution of orientations**



**Stabilization and recovery time based on distribution of orientations**

**E-field aligned with non-preferred direction**



**Slower stabilization and recovery time**

**Built-in E-field**



**Figure 6. Effect of crystal orientation on ion migration.** Schematic drawing showing the impact of crystal orientation alignment with the built-in electric field in devices. The change in ion migration energy barrier could lead to variation in the time needed to achieve steady state operation and to re-establish dark condition equilibrium.

It should be noted that both the thin film and single crystal samples are terminated with the (010) plane at the surface.<sup>33, 35</sup> In contrast, polycrystalline films used in devices may have crystalline grains with orientations that vary from grain to grain,<sup>44, 45</sup> which could result in different migration energies. The dependence of the migration energy on the direction of migration has important consequences for perovskite devices, which are made from polycrystalline films with grains of varying orientation. Specifically, the orientation of the individual grains with respect to the vertical axis of the device, along which the built-in electric field occurs, will affect paths along which ions migrate under illumination and subsequently diffuse back to equilibrium during dark conditions (*i.e.*, at night). The paths along different crystal directions will have different migration energies, and thus different time constants for achieving steady state operation and for returning back to dark condition equilibrium (Fig. 6). It has been reported that perovskite solar cells have reversible losses under illumination due to cation migration, and that a certain recovery time in the dark is needed to return to original efficiency.<sup>24</sup> This recovery time depends on the energy barrier for ions to diffuse back to equilibrium, which would be affected by the distribution of grain orientations. Identifying a specific orientation that enables quick device recovery could provide a valuable research avenue for creating perovskite solar cells that have an overall higher performance, better stability and are well suited to locations with rapidly changing sun irradiance.

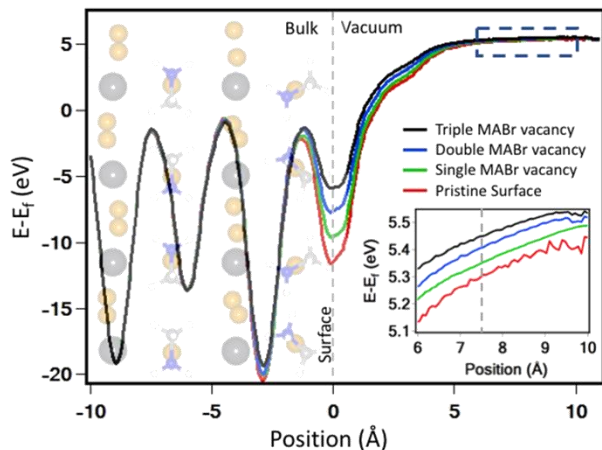


**Figure 7. Surface defect-induced work function modification.** Electric potential plotted as a function of position relative to the surface. Position of -10 Å corresponds to the bottom of the slab. (Inset) Zoom on the vacuum region to highlight differences in the work function. After linear fitting, the work function was taken to be the potential value (relative to the Fermi energy) at a distance of 7.5 Å (grey dotted line).

In addition to the dynamics of intrinsic defect species and the mechanisms of defect-assisted ion migration, it is also of interest to understand how the surface defects observed in STM affect the surface properties of the perovskite, which would in turn affect the interface of the perovskite with an adjacent layer in a device. Such interfaces are seen as a key to optimizing device performance, as they play an important role in charge transport and recombination. To better understand the effect of these vacancies on the interface, the electronic potential was calculated as a function of position along the axis normal to the perovskite surface (Fig. 7). Significant separation of the poten-

tial curves occurs around 0 Å, which corresponds to the perovskite surface. This may be due to defect energy levels introduced by dangling bonds. The inset of Fig. 7 shows in detail the area used for identifying the vacuum level. A linear fit was used, and the value of this fit at 7.5 Å (middle of the vacuum slab) was taken to be the vacuum level. This also determines the work function, which is the difference in energy between the Fermi level and the vacuum level. Importantly, a trend was identified in which an increasing number of vacancies raised the work function from 5.29 eV (pristine surface) to 5.45 eV (triple MABr vacancy).

It is important to note that the size of the super cell used for the calculation is limited. For the pristine surface there are 8 Br<sup>-</sup> ions and 8 MA<sup>+</sup> cations in the surface layer of the supercell used for DFT. Thus, the single, double, and triple MABr vacancy defect surfaces have 1/8, 2/8 and 3/8 of the atoms missing and correspond to an overall MABr surface vacancy defect concentration of 12.5%, 25%, and 37.5%, respectively. It has been suggested that ion migration leaves one end of the perovskite film deficient in the migrating halide species (*i.e.*, rich in halide vacancies).<sup>28</sup> Thus, such high defect concentrations may occur at the interface during device operation. Additionally, the variation of the local work function could potentially alter charge transfer to adjacent layers (*i.e.*, electron or hole transport layers, top electrode) in a solar cell or light emitting device. It is important to take this effect into account when evaluating efficiency loss mechanisms. Understanding interfaces in perovskite devices, and engineering energy level alignment between layers, has been identified as one of the keys to unlocking higher efficiencies and better stability.<sup>46</sup> As further work on energy level alignment between layers is conducted, it should be kept in mind that this work function variation at the interface exists due to surface defects. This variation may limit the accuracy of energy level alignment attainable if the issue of reducing or controlling the number of defects in the perovskite film is not addressed. As seen in the migration mechanisms investigated, there could be spatial variation in work function not only due to the presence of defects but also spatial and temporal variation as vacancies migrate to and from the surface, as well as along the surface. Such variation of the electronic properties of perovskite in space and in time could in turn affect the charge transfer at the interface.

## CONCLUSION

We present an atomic-scale investigation of defect dynamics in organic-inorganic hybrid perovskite by combining experimental techniques (STM) and theoretical calculations (DFT). Scanning tunneling microscopy allowed us to visualize the motion of a single ion in real space and real time. Additionally, density functional theory calculations were performed to identify the chemical origin of defects and the path used by ions to migrate. Multiple defect types were observed by STM at the surface of MAPbBr<sub>3</sub> perovskite, including vacancy clusters and unpaired Br<sup>-</sup> defects. Vacancy defects were identified as MABr vacancies according to DFT calculations. Several dynamic phenomena were observed, including reorientation of Br<sup>-</sup> pairs, and vacancy movement both in the z-direction as well as along the surface. Movement of defects to and from the surface (*i.e.*, z-direction) corresponds to the motion expected from the ion migration phenomenon in OHPs. Our results strongly support the hypothesis of a vacancy-assisted ion migration pathway in per-

ovskite materials. In addition, we demonstrate that in the z-direction it is energetically favorable for MABr migration to occur *via* a sequential mechanism. The transition energy barrier we found is small enough for ion migration to occur *via* this mechanism in an operating perovskite solar cell. Furthermore, we revealed the impact of vacancy defects on the local work function at the surface of the perovskite. The modification of local work function induced by clusters of vacancies observed here is expected to strongly affect charge transport and recombination at the interface of a device. Here we revealed the nature and dynamics of defects in MAPbBr<sub>3</sub> at the atomic scale. Our study not only provides fundamental understanding of the effect of vacancy defects at the perovskite surface, but also provides a microscopic insight into the ion migration mechanism. Equally important, our work reveals useful information for device improvement from the perspective of defects and interface engineering.

## METHODS

**Surface characterization.** Both single crystal and thin film perovskite samples were used for this study. Within the resolution of the STM, no difference was distinguishable in terms of defect nature, defect prevalence or ion transport behavior between the single crystal and thin film samples. STM images in Figs. 1 and 2 were taken on a single crystal sample. STM images in Figs. 3 and 4 were taken on a thin-film sample. MAPbBr<sub>3</sub> single crystal samples were grown *via* the solvent exchange method<sup>47</sup> and then cleaved *in situ* in ultrahigh vacuum (UHV) environment (10<sup>-9</sup> torr) with a scalpel to obtain a pristine surface. MAPbBr<sub>3</sub> thin film perovskite was grown on the surface of an Au (111) single crystal by dual-source vacuum co-evaporation. First, the gold sample was cleaned in UHV environment (10<sup>-9</sup> torr), by several cycles of Ne<sup>+</sup> sputtering followed by subsequent annealing at 773 K for 5 min. Thereafter, MAPbBr<sub>3</sub> was obtained by co-evaporation of MABr and PbBr<sub>2</sub> species at evaporation temperatures of 361 K and 498 K respectively for 10 min. During evaporation, the gold surface was kept at 130 K to ensure the sticking of the methyl-ammonium compound. Low-temperature scanning tunneling microscope (LT-STM) was used to characterize the atomic-scale structures of the different perovskite samples. The STM measurements were performed at a range of temperatures (4.6K-180K), which were achieved by cooling with either liquid nitrogen or liquid helium followed by counter heating *via* a Lakeshore 335 Temperature Controller connected to the STM sample stage. Cut Pt/Ir tips were used to acquire the STM images. The bias voltage was applied to the sample. It has been reported that high-energy electrons from the tip can induce surface degradation under UHV conditions in single crystal MAPbBr<sub>3</sub> during conductive AFM imaging.<sup>48</sup> To verify that our STM imaging did not induce generation and diffusion of atomic defects and surface degradation during the imaging process, we scanned the same area consecutively for 117 times, and no surface degradation or defect generation was observed. Additionally, the effect of the tip on diffusion events has been previously shown to be negligible when using the “movie” technique of taking consecutive images of the same area.<sup>49</sup>

**Density functional theory.** Density functional theory<sup>50,51</sup> (DFT) calculations were performed using the Vienna *ab initio*

simulation package<sup>52,53</sup> (VASP) code. The projector augmented wave (PAW) pseudopotential<sup>54,55</sup> was used to describe the core electrons and a plane wave basis set with a kinetic energy cutoff of 400 eV was used to expand the wave functions. Electronic exchange and correlation was described within the framework of generalized gradient approximation (GGA) of Perdew, Burke and Ernzerhof (PBE) functionals.<sup>56</sup> The MAPbBr<sub>3</sub> (010) surface was represented using a periodic slab based on the space group Pnma containing four atomic layers and a vacuum thickness of 14 Å. Specifically, two supercells were used, one is a 2 × 2 supercell used for the vacancy calculations, while the other is a 3 × 1 supercell for the dimer orientation shift calculations. Respectively, Brillouin zone (BZ) sampling was done using 3 × 1 × 3 and 6 × 1 × 2 Monkhorst–Pack<sup>57</sup> grids. The bottom layer of atoms was kept fixed, while the other atoms were allowed to relax. All structures were fully relaxed until the force on each atom was less than 0.01 eV/Å. Transition states for MABr migration along the surface were located by climbing image nudged elastic band (CI-NEB) method<sup>58</sup> using three images with a convergence of 0.05 eV/Å for the force components both along and perpendicular to the tangent of the reaction path.

## ASSOCIATED CONTENT

### Supporting Information:

Figs. S1-S8 and Table S1 providing information on calculation supercells, Van der Waals correction comparison, Br<sup>-</sup> pair reorientation transition energies, Br<sup>-</sup> pair separation energy, long range reorientation images, bulk to surface ion transport, and energy curves and crystal structures for sequential and simultaneous ion transport mechanisms. Supplemental movies 1 and 2 show Br<sup>-</sup> pair reorientation and ion transport events.

This material is available free of charge *via* the internet at <http://pubs.acs.org>.

The authors declare no competing financial interest.

## AUTHOR INFORMATION

### Corresponding Authors

\* Yabing Qi, [Yabing.Qi@OIST.jp](mailto:Yabing.Qi@OIST.jp)

\* Guofeng Wang, [guw8@pitt.edu](mailto:guw8@pitt.edu)

### Present Addresses

#Department Physik, Universität Siegen, 57068 Siegen, Germany.

### ORCID IDs

Collin Stecker: 0000-0003-4247-5699

Jeremy Hieulle: 0000-0003-4891-4007

Robin Ohmann: 0000-0003-2483-1282

Luis K. Ono: 0000-0003-3176-1876

Yabing Qi: 0000-0002-4876-8049

### Author Contributions

<sup>§</sup>C.S. and K.L. contributed equally.

## ACKNOWLEDGMENT

This work was supported by funding from the Energy Materials and Surface Sciences Unit of the Okinawa Institute of Science and Technology Graduate University, the OIST R&D Cluster Research Program, the OIST Proof of Concept (POC) Program, and JSPS KAKENHI Grant Number JP18K05266. G. Wang gratefully acknowledges the computational resources provided by the University of Pittsburgh Center for Research Computing as well as the

## REFERENCES

- (1) National Renewable Energy Laboratory (NREL) Solar Cell Efficiency Chart. <https://www.nrel.gov/pv/assets/pdfs/best-research-cell-efficiencies.20190923.pdf> (accessed 09/24/2019).
- (2) Shao, Y.; Xiao, Z.; Bi, C.; Yuan, Y.; Huang, J. Origin and Elimination of Photocurrent Hysteresis by Fullerene Passivation in CH<sub>3</sub>NH<sub>3</sub>PbI<sub>3</sub> Planar Heterojunction Solar Cells. *Nat. Commun.* **2014**, *5*, 5784.
- (3) Miller, D. W.; Eperon, G. E.; Roe, E. T.; Warren, C. W.; Snaith, H. J.; Loneragan, M. C. Defect States in Perovskite Solar Cells Associated with Hysteresis and Performance. *Appl. Phys. Lett.* **2016**, *109*, 153902.
- (4) Liu, Z.; Hu, J.; Jiao, H.; Li, L.; Zheng, G.; Chen, Y.; Huang, Y.; Zhang, Q.; Shen, C.; Chen, Q.; Zhou, H. Chemical Reduction of Intrinsic Defects in Thicker Heterojunction Planar Perovskite Solar Cells. *Adv. Mater.* **2017**, *29*, 1606774.
- (5) Ball, J. M.; Petrozza, A. Defects in Perovskite-Halides and Their Effects in Solar Cells. *Nat. Energy* **2016**, *1*, 16149.
- (6) Wang, L. G.; Zhou, H. P.; Hu, J. N.; Huang, B. L.; Sun, M. Z.; Dong, B. W.; Zheng, G. H. J.; Huang, Y.; Chen, Y. H.; Li, L.; Xu, Z. Q.; Li, N. X.; Liu, Z.; Chen, Q.; Sun, L. D.; Yan, C. H. A Eu<sup>3+</sup>-Eu<sup>2+</sup> Ion Redox Shuttle Imparts Operational Durability to Pb-I Perovskite Solar Cells. *Science* **2019**, *363*, 265—270.
- (7) Zhang, F.; Bi, D. Q.; Pellet, N.; Xiao, C. X.; Li, Z.; Berry, J. J.; Zakeeruddin, S. M.; Zhu, K.; Grätzel, M. Suppressing Defects through the Synergistic Effect of a Lewis Base and a Lewis Acid for Highly Efficient and Stable Perovskite Solar Cells. *Energy Environ. Sci.* **2018**, *11*, 3480—3490.
- (8) Lin, C. T.; De Rossi, F.; Kim, J.; Baker, J.; Ngiam, J.; Xu, B.; Pont, S.; Aristidou, N.; Haque, S. A.; Watson, T.; McLachlan, M. A.; Durrant, J. R. Evidence for Surface Defect Passivation as the Origin of the Remarkable Photostability of Unencapsulated Perovskite Solar Cells Employing Aminovaleric Acid as a Processing Additive. *J. Mater. Chem. A* **2019**, *7*, 3006—3011.
- (9) Zheng, X. P.; Deng, Y. H.; Chen, B.; Wei, H. T.; Xiao, X.; Fang, Y. J.; Lin, Y. Z.; Yu, Z. H.; Liu, Y.; Wang, Q.; Huang, J. S. Dual Functions of Crystallization Control and Defect Passivation Enabled by Sulfonic Zwitterions for Stable and Efficient Perovskite Solar Cells. *Adv. Mater.* **2018**, *30*, 1803428.
- (10) Wu, Z. F.; Raga, S. R.; Juarez-Perez, E. J.; Yao, X. Y.; Jiang, Y.; Ono, L. K.; Ning, Z. J.; Tian, H.; Qi, Y. B. Improved Efficiency and Stability of Perovskite Solar Cells Induced by C=O Functionalized Hydrophobic Ammonium-Based Additives. *Adv. Mater.* **2018**, *30*, 1703670.
- (11) Wang, S.; Jiang, Y.; Juarez-Perez, Emilio J.; Ono, Luis K.; Qi, Y. B. Accelerated Degradation of Methylammonium Lead Iodide Perovskites Induced by Exposure to Iodine Vapour. *Nat. Energy* **2016**, *2*, 16195.
- (12) Juarez-Perez, E. J.; Ono, L. K.; Maeda, M.; Jiang, Y.; Hawash, Z.; Qi, Y. B. Photodecomposition and Thermal Decomposition in Methylammonium Halide Lead Perovskites and Inferred Design Principles to Increase Photovoltaic Device Stability. *J. Mater. Chem. A* **2018**, *6*, 9604—9612.
- (13) Xu, J.; Buin, A.; Ip, A. H.; Li, W.; Voznyy, O.; Comin, R.; Yuan, M. J.; Jeon, S.; Ning, Z. J.; McDowell, J. J.; Kanjanaboos, P.; Sun, J. P.; Lan, X. Z.; Quan, L. N.; Kim, D. H.; Hill, I. G.; Maksymovych, P.; Sargent, E. H. Perovskite-Fullerene Hybrid Materials Suppress Hysteresis in Planar Diodes. *Nat. Commun.* **2015**, *6*, 7081.
- (14) Buin, A.; Pietsch, P.; Xu, J. X.; Voznyy, O.; Ip, A. H.; Comin, R.; Sargent, E. H. Materials Processing Routes to Trap-Free Halide Perovskites. *Nano Lett.* **2014**, *14*, 6281—6286.
- (15) Yin, W.-J.; Shi, T.; Yan, Y. Unusual Defect Physics in CH<sub>3</sub>NH<sub>3</sub>PbI<sub>3</sub> Perovskite Solar Cell Absorber. *Appl. Phys. Lett.* **2014**, *104*, 063903.
- (16) Baumann, A.; Vath, S.; Rieder, P.; Heiber, M. C.; Tvingstedt, K.; Dyakonov, V. Identification of Trap States in Perovskite Solar Cells. *J. Phys. Chem. Lett.* **2015**, *6*, 2350—2354.
- (17) Gordillo, G.; Otalora, C. A.; Ramirez, A. A. A Study of Trap and Recombination Centers in MAPbI<sub>3</sub> Perovskites. *Phys. Chem. Chem. Phys.* **2016**, *18*, 32862—32867.
- (18) Yin, W. J.; Shi, T. T.; Yan, Y. F. Unique Properties of Halide Perovskites as Possible Origins of the Superior Solar Cell Performance. *Adv. Mater.* **2014**, *26*, 4653—4658.
- (19) Walsh, A.; Scanlon, D. O.; Chen, S. Y.; Gong, X. G.; Wei, S. H. Self-Regulation Mechanism for Charged Point Defects in Hybrid Halide Perovskites. *Angew. Chem. Int. Edit.* **2015**, *54*, 1791—1794.
- (20) Kim, J.; Lee, S. H.; Lee, J. H.; Hong, K. H. The Role of Intrinsic Defects in Methylammonium Lead Iodide Perovskite. *J. Phys. Chem. Lett.* **2014**, *5*, 1312—1317.
- (21) Eames, C.; Frost, J. M.; Barnes, P. R. F.; O'Regan, B. C.; Walsh, A.; Islam, M. S. Ionic Transport in Hybrid Lead Iodide Perovskite Solar Cells. *Nat. Commun.* **2015**, *6*, 7497.
- (22) Yuan, Y. B.; Chae, J.; Shao, Y. C.; Wang, Q.; Xiao, Z. G.; Centrone, A.; Huang, J. S. Photovoltaic Switching Mechanism in Lateral Structure Hybrid Perovskite Solar Cells. *Adv. Energy Mater.* **2015**, *5*, 1500615.
- (23) Yuan, Y. B.; Huang, J. S. Ion Migration in Organometal Trihalide Perovskite and Its Impact on Photovoltaic Efficiency and Stability. *Acc. Chem. Res.* **2016**, *49*, 286—293.
- (24) Domanski, K.; Roose, B.; Matsui, T.; Saliba, M.; Turren-Cruz, S.-H.; Correa-Baena, J.-P.; Carmona, C. R.; Richardson, G.; Foster, J. M.; De Angelis, F.; Ball, J. M.; Petrozza, A.; Mine, N.; Nazeeruddin, M. K.; Tress, W.; Grätzel, M.; Steiner, U.; Hagfeldt, A.; Abate, A. Migration of Cations Induces Reversible Performance Losses over Day/Night Cycling in Perovskite Solar Cells. *Energy Environ. Sci.* **2017**, *10*, 604—613.
- (25) Snaith, H. J.; Abate, A.; Ball, J. M.; Eperon, G. E.; Leijtens, T.; Noel, N. K.; Stranks, S. D.; Wang, J. T.; Wojciechowski, K.; Zhang, W. Anomalous Hysteresis in Perovskite Solar Cells. *J. Phys. Chem. Lett.* **2014**, *5*, 1511—1515.
- (26) Unger, E. L.; Hoke, E. T.; Bailie, C. D.; Nguyen, W. H.; Bowring, A. R.; Heumüller, T.; Christoforo, M. G.; McGehee, M. D. Hysteresis and Transient Behavior in Current-Voltage Measurements of Hybrid-Perovskite Absorber Solar Cells. *Energy Environ. Sci.* **2014**, *7*, 3690—3698.
- (27) Yuan, Y. B.; Wang, Q.; Shao, Y. C.; Lu, H. D.; Li, T.; Gruverman, A.; Huang, J. S. Electric-Field-Driven Reversible Conversion between Methylammonium Lead Triiodide Perovskites and Lead Iodide at Elevated Temperatures. *Adv. Energy Mater.* **2016**, *6*, 1501803.
- (28) Li, C.; Tscheuschner, S.; Paulus, F.; Hopkinson, P. E.; Kiessling, J.; Kohler, A.; Vaynzof, Y.; Huettner, S. Iodine Migration and Its Effect on Hysteresis in Perovskite Solar Cells. *Adv. Mater.* **2016**, *28*, 2446—2454.
- (29) Bag, M.; Renna, L. A.; Adhikari, R. Y.; Karak, S.; Liu, F.; Lahti, P. M.; Russell, T. P.; Tuominen, M. T.; Venkataraman, D. Kinetics of Ion Transport in Perovskite Active Layers and Its Implications for Active Layer Stability. *J. Am. Chem. Soc.* **2015**, *137*, 13130—13137.
- (30) De Bastiani, M.; Dell'Erba, G.; Gandini, M.; D'Innocenzo, V.; Neutzner, S.; Kandada, A. R. S.; Grancini, G.; Binda, M.; Prato, M.; Ball, J. M.; Caironi, M.; Petrozza, A. Ion Migration and the Role of Preconditioning Cycles in the Stabilization of the J-V Characteristics of Inverted Hybrid Perovskite Solar Cells. *Adv. Energy Mater.* **2016**, *6*, 1501453.
- (31) Yang, Y.; Yang, M.; Moore, David T.; Yan, Y.; Miller, Elisa M.; Zhu, K.; Beard, Matthew C. Top and Bottom Surfaces Limit Carrier Lifetime in Lead Iodide Perovskite Films. *Nat. Energy* **2017**, *2*, 16207.
- (32) Hieulle, J.; Stecker, C.; Ohmann, R.; Ono, L. K.; Qi, Y. B. Scanning Probe Microscopy Applied to Organic-Inorganic Halide Perovskite Materials and Solar Cells. *Small Methods* **2018**, *2*, 1700295.
- (33) Ohmann, R.; Ono, L. K.; Kim, H. S.; Lin, H.; Lee, M. V.; Li, Y.; Park, N. G.; Qi, Y. B. Real-Space Imaging of the Atomic Structure of Organic-Inorganic Perovskite. *J. Am. Chem. Soc.* **2015**, *137*, 16049—16054.
- (34) She, L.; Liu, M.; Zhong, D., Atomic Structures of CH<sub>3</sub>NH<sub>3</sub>PbI<sub>3</sub> (001) Surfaces. *ACS Nano* **2016**, *10*, 1126—1131.
- (35) Hieulle, J.; Wang, X. M.; Stecker, C.; Son, D. Y.; Qu, L. B.; Ohmann, R.; Ono, L. K.; Mugarza, A.; Yan, Y. F.; Qi, Y. B. Unraveling

- the Impact of Halide Mixing on Perovskite Stability. *J. Am. Chem. Soc.* **2019**, *141*, 3515—3523.
- (36) Hsu, H.-C.; Huang, B.-C.; Chin, S.-C.; Hsing, C.-R.; Nguyen, D.-L.; Schnedler, M.; Sankar, R.; Dumin-Borkowski, R. E.; Wei, C.-M.; Chen, C.-W.; Ebert, P.; Chiu, Y.-P. Photodriven Dipole Reordering: Key to Carrier Separation in Metalorganic Halide Perovskites. *ACS Nano* **2019**, *13*, 4402—4409.
- (37) Knorr, N.; Brune, H.; Epple, M.; Hirstein, A.; Schneider, M. A.; Kern, K. Long-Range Adsorbate Interactions Mediated by a Two-Dimensional Electron Gas. *Phys. Rev. B* **2002**, *65*, 115420.
- (38) Azpiroz, J. M.; Mosconi, E.; Bisquert, J.; De Angelis, F. Defect Migration in Methylammonium Lead Iodide and Its Role in Perovskite Solar Cell Operation. *Energy Environ. Sci.* **2015**, *8*, 2118—2127.
- (39) Liu, Y.; Palotas, K.; Yuan, X.; Hou, T.; Lin, H.; Li, Y.; Lee, S. T. Atomistic Origins of Surface Defects in CH<sub>3</sub>NH<sub>3</sub>PbBr<sub>3</sub> Perovskite and Their Electronic Structures. *ACS Nano* **2017**, *11*, 2060—2065.
- (40) Pramchu, S.; Cheiwchanchamnangij, T.; Laosiritaworn, Y.; Jaroenjittichai, A. P. Enhancing Surface Stabilization of CH<sub>3</sub>NH<sub>3</sub>PbI<sub>3</sub> Perovskite by Cl and Br Doping: First-Principles Study. *J. Appl. Phys.* **2019**, *125*, 115302.
- (41) Gustafsson, A.; Okabayashi, N.; Peronio, A.; Giessibl, F. J.; Paulsson, M. Analysis of STM Images with Pure and Co-Functionalized Tips: A First-Principles and Experimental Study. *Phys. Rev. B* **2017**, *96*, 085415.
- (42) Walsh, A.; Stranks, S. D., Taking Control of Ion Transport in Halide Perovskite Solar Cells. *ACS Energy Lett.* **2018**, *3*, 1983—1990.
- (43) Zhang, Y. P.; Wang, Y. S.; Xu, Z. Q.; Liu, J. Y.; Song, J. C.; Xue, Y. Z.; Wang, Z. Y.; Zheng, J. L.; Jiang, L. C.; Zheng, C. X.; Huang, F. Z.; Sun, B. Q.; Cheng, Y. B.; Bao, Q. L. Reversible Structural Swell-Shrink and Recoverable Optical Properties in Hybrid Inorganic-Organic Perovskite. *ACS Nano* **2016**, *10*, 7031—7038.
- (44) Leblebici, S. Y.; Leppert, L.; Li, Y.; Reyes-Lillo, S. E.; Wickenburg, S.; Wong, E.; Lee, J.; Melli, M.; Ziegler, D.; Angell, D. K.; Ogletree, D. F.; Ashby, Paul D.; Toma, F. M.; Neaton, J. B.; Sharp, I. D.; Weber-Bargioni, A. Facet-Dependent Photovoltaic Efficiency Variations in Single Grains of Hybrid Halide perovskite. *Nat. Energy* **2016**, *1*, 16093.
- (45) Kim, D. H.; Park, J.; Li, Z.; Yang, M. J.; Park, J. S.; Park, I. J.; Kim, J. Y.; Berry, J. J.; Rumbles, G.; Zhu, K. 300% Enhancement of Carrier Mobility in Uniaxial-Oriented Perovskite Films Formed by Topotactic-Oriented Attachment. *Adv. Mater.* **2017**, *29*, 1606831.
- (46) Ono, L. K.; Qi, Y. B. Surface and Interface Aspects of Organometal Halide Perovskite Materials and Solar Cells. *J. Phys. Chem. Lett.* **2016**, *7*, 4764—4794.
- (47) Tidhar, Y.; Edri, E.; Weissman, H.; Zohar, D.; Hodes, G.; Cahen, D.; Rybtchinski, B.; Kirmayer, S. Crystallization of Methyl Ammonium Lead Halide Perovskites: Implications for Photovoltaic Applications. *J. Am. Chem. Soc.* **2014**, *136*, 13249—13256.
- (48) Choi, J. I. J.; Khan, M. E.; Hawash, Z.; Kim, K. J.; Lee, H.; Ono, L. K.; Qi, Y. B.; Kim, Y.-H.; Park, J. Y. Atomic-Scale View of Stability and Degradation of Single-Crystal MAPbBr<sub>3</sub> Surfaces. *J. Mater. Chem. A* **2019**, *7*, 20760—20766.
- (49) Fomin, E.; Tatarikhonov, M.; Mitsui, T.; Rose, M.; Ogletree, D.; Salmeron, M. Vibrationally Assisted Diffusion of H<sub>2</sub>O and D<sub>2</sub>O on Pd(111). *Surface Science* **2006**, *600*, 542—546.
- (50) Kohn, W.; Sham, L. J. Self-Consistent Equations Including Exchange and Correlation Effects. *Phys. Rev.* **1965**, *140*, 1133—1138.
- (51) Hohenberg, P.; Kohn, W. Inhomogeneous Electron Gas. *Phys. Rev. B* **1964**, *136*, 864—871.
- (52) Kresse, G.; Hafner, J. *Ab Initio* Molecular Dynamics for Liquid Metals. *Phys. Rev. B* **1993**, *47*, 558—561.
- (53) Kresse, G.; Furthmüller, J. Efficiency of *Ab Initio* Total Energy Calculations for Metals and Semiconductors Using a Plane-Wave Basis Set. *Comp. Mater. Sci.* **1996**, *6*, 15—50.
- (54) Kresse, G.; Joubert, D. From ultrasoft pseudopotentials to the projector augmented-wave method. *Phys. Rev. B* **1999**, *59*, 1758—1775.
- (55) Blochl, P. E. Projector Augmented-Wave Method. *Phys. Rev. B* **1994**, *50*, 17953—17979.
- (56) Perdew, J. P.; Burke, K.; Ernzerhof, M. Generalized Gradient Approximation Made Simple. *Phys. Rev. Lett.* **1996**, *77*, 3865—3868.
- (57) Monkhorst, H. J.; Pack, J. D. Special Points for Brillouin-Zone Integrations. *Phys. Rev. B* **1976**, *13*, 5188—5192.
- (58) Henkelman, G.; Uberuaga, B. P.; Jonsson, H. A Climbing Image Nudged Elastic Band Method for Finding Saddle Points and Minimum Energy Paths. *J. Chem. Phys.* **2000**, *113*, 9901—9904.

TOC Figure

